Computational and Structural Biotechnology Journal 20 (2022) 4157–4171

COMPUTATIONAL ANDSTRUCTURAL BIOTECHNOLOGY JOURNAL

journal homepage: www.elsevier.com/locate/csbj

Molecular and structural basis of actin filament severing by ADF/cofilin

Sharad V. Jaswandkar, Kalpana S. Katti, Dinesh R. Katti *

Department of Civil, Construction and Environmental Engineering, North Dakota State University, Fargo, ND 58105, United States

ARTICLE INFO

Article history:
Received 25 May 2022
Received in revised form 30 July 2022
Accepted 31 July 2022
Available online 4 August 2022

Keywords:
Actin
ADF/cofilin
molecular dynamics
actin dynamics
cytoskeleton

ABSTRACT

ADF/cofilin's cooperative binding to actin filament modifies the conformation and alignment of G-actin subunits locally, causing the filament to sever at "boundaries" formed among bare and ADF/cofilin-occupied regions. Analysis of the impact of the ADF/cofilin cluster boundary on the deformation behavior of actin filaments in a mechanically strained environment is critical for understanding the biophysics of their severing. The present investigation uses molecular dynamics simulations to generate atomic resolution models of bare, partially, and fully cofilin decorated actin filaments. Steered molecular dynamics simulations are utilized to determine the mechanical properties of three filament models when subjected to axial stretching, axial compression, and bending forces. We highlight differences in strain distribution, failure mechanisms in the three filament models, and biomechanical effects of cofilin cluster boundaries in overall filament rupture. Based on the influence of ADF/cofilin binding on intrastrand and interstrand G-actin interfaces, the cofilin-mediated actin filament severing model proposed here can help understand cofilin mediated actin dynamics.

1. Introduction

Actin is among the most abundant intracellular proteins found in all eukaryotic cells. The dynamic remodeling of an actin cytoskeleton is involved in many cellular processes such as cell motility, cytokinesis, tumor cell transformation, and metastasis [1–3]. The actin filament (F-actin), a linear, helical, and polar polymer formed by the head-to-tail assemblage of actin monomers (G-actin subunits), is the central element of the actin cytoskeleton. The actin cytoskeleton assembly dynamics and architecture are modulated spatially and temporally through regulatory actin-binding proteins [4]. Members of the actin-depolymerizing factor (ADF)/cofilin protein family are the severing proteins responsible for F-actin disassembly [2,5,6].

All eukaryotes express ADF/cofilin (hereafter referred to as "cofilin") that plays a critical role in speeding up the actin cytoskeleton remodeling [7], impacting the dynamics of motile structures like lamellipodia [8], listeria comet tails [9], neural growth cones [10], and filopodia [6]. Cofilin, by modulating the quantity and length of actin filaments, also aids in the normal functioning of contractile systems such as stress fibers [11], contractile rings [12], and muscles [13]. Cofilin binds to F-actin between two adjacent G-actin subunits along the helical strands forming what is known as a decorative contact or cofilin decoration [14]. Cofilin favorably interacts with ADP-G-actin instead of ADP-Pi-G-actin or ATP-G-actin [15,16] and attaches cooperatively to F-actin [17,18], forming a cofilin cluster [19,20] (henceforth referred to as a "cluster"). Cofilin occupancy affects F-actin twist [21], subunits tilt [22,23], making it more flexible in bending [24] and twisting [25]. Our recent study found that F-actin's mechanical properties are governed by the atomic-scale structure of the contact interface between G-actin subunits [26]. Therefore, to understand cofilin-mediated F-actin severing, it is crucial to understand cofilin-linked changes in filament structure at G-actin-G-actin interfaces. Prior structural and biochemical experimental studies on F-actin demonstrated that F-actins partially decorated with cofilin severs at the junctions formed between bare and cofilin-decorated segments [27,28] (hereafter referred to as "cluster boundaries"). The boundaries of the cofilin decorated region (cluster) are not structurally similar; it has been observed that the pointy end side of the cluster severs at a higher rate than the barbed end side [29,30]. In contrast, some prior studies also show that actin filaments with small cofilin clusters are likely to fracture within the flexible cofilin-actin region rather than at boundaries [31]. Cofilin cluster causes the formation of two distinct segments along the filament length: cofilin decorated segment and bare F-actin segment. The cofilin decorated segment situate between the bare F-actin

* Corresponding author.
E-mail address: Dinesh.Katti@ndsu.edu (D.R. Katti).

https://doi.org/10.1016/j.csbj.2022.07.054

segments at the pointed end and barbed end side. In many cellular activities, actin filaments are exposed to a variety of mechanical constraints, resulting in bending, axial tensile, and compression deformations. The nature and magnitude of mechanical stress imposed on individual F-actins depend on the architecture of the actin network and their orientation within it. The structural heterogeneity in the filament generated by the cofilin cluster may have a role in strain concentration, fracture risk, and damage accumulation along the F-actin during mechanical deformation. Previous structural investigations on cofilin decorated F-actin (also known as "cofilactin") were limited to demonstrating the structural changes caused by cofilin in F-actin that promote its severing [22,32,33]. However, how the mechanically strained environment combined with cofilin-linked structural alterations contribute to F-actin severing mechanics has not been thoroughly investigated. The current study provides insights into the molecular mechanisms and dynamics that promote F-actin severing at cofilin cluster boundaries under different loading conditions, namely tension, compression, and bending. Molecular dynamics (MD) simulations have successfully captured the molecular features of proteins [34–37], including cofilin-linked changes in F-actin structure. In this paper, we utilize MD simulations to predict the structural features of cofilin cluster boundaries. Furthermore, the steered molecular dynamics (SMD) simulations are used to mimic the structural evolution of these boundaries and the severing process dynamics under various deformation modes. We show that the nanostructural spatial heterogeneity produced by the cofilin-decorated segment leads to the formation of locally fragile regions that facilitate F-actin severing. SMD simulation of partial and fully cofilin-decorated F-actin models allowed us to analyze and track the effects of loading rate and loading conditions on the biophysics of F-actin severing by ADF/cofilin.

2. Materials and methods

2.1. Construction of actin filament models

The molecular model of bare F-actin was built based on a cryo-electron microscopic (EM) structure obtained from a protein data bank (PDB ID: 3LUE) [38]. Cofilin mainly interacts with ADP-F-actin instead of ATP-F-actin [17,39]. Therefore, for the bare F-actin model simulations with ADP, ADP coordinates from the ADP G-actin PDB entry 1J6Z [40] were used. The ADP-F-actin model consisting of ten G-actin subunits was first minimized and equilibrated for 15 ns using MD simulations (Fig. 1a). Then, the cofilin decorated structure of F-actin was constructed based on the available cryo-EM structure of ADF/cofilin (PDB ID: 3J0S) [22]. The PDB code 3J0S is a cryo-EM three-dimensional reconstruct of the cofilin-decorated F-actin. To comprehend the impact of the cofilin binding on mechanical properties and deformation behavior of F-actin. A fully cofilin decorated actin filament structure (FCDA filament) was constructed by replacing the initial actin filament structures in 3J0S with the minimized and equilibrated ADP F-actin structure using UCSF Chimera. Fig. 1c represents a full cofilin decorated F-actin structure consisting of ten G-actin subunits and eight cofilin monomers.

To investigate the molecular mechanism of actin filament severing at boundaries between bare and cofilin-decorated segments, the partially cofilin decorated actin filament (PCDA filament) structure was constructed using four cofilin monomers forming a cluster on ten subunit ADP F-actin, as shown in Fig. 1b. The structures and coordinate files of bare F-actin, PCDA, and FCDA filaments were produced using Nanoscale Molecular Dynamics (NAMD) psfgen tool [41], by utilizing topology and force-field parameter files obtained from chemistry at Harvard Molecular Mechanics

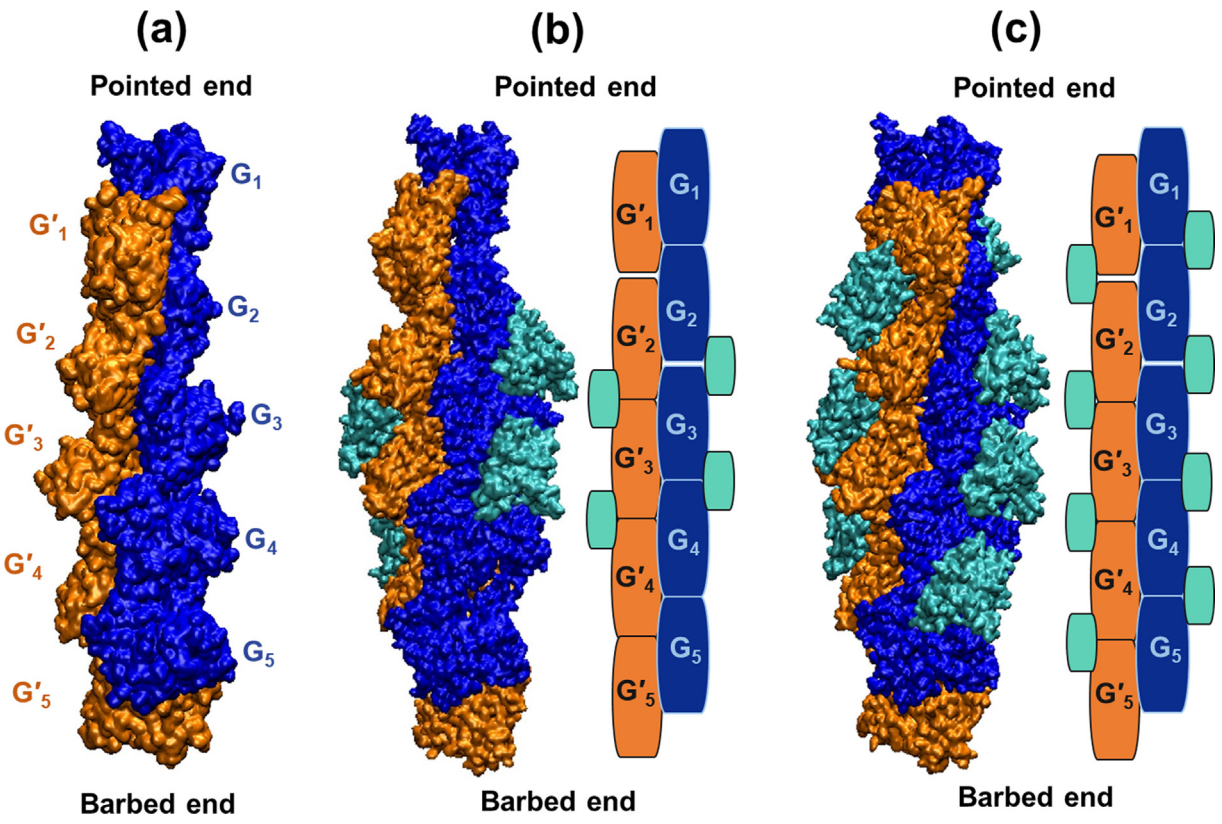

Fig. 1. Computationally generated bare F-actin and cofilactin filament models and labeling convention. (a) Ten subunits double-stranded structure of bare F-actin designated as strands G′ (orange) and G (blue) and G-actin subunits are labeled in a natural numbers sequence from the pointed (-) end. (b-c) The atomic structure and schematic illustration of cofilactin filaments consist of four and eight cofilin subunits forming PCDA (b) and FCDA (c) filament models.

(CHARMM) [42]. Using the VMD plugin, all the filament models were placed in a water box to solvate (the TIP3P force field for the water model). The system was then brought to electrostatic neutrality utilizing the VMD autoionize function. All simulations were carried out using the NAMD software package [43] and the CHARMM36 force fields. The conjugate gradient approach is used for energy minimization of the filament models. The temperature and pressure of the solvated filament structures were raised to 300 K and 1.01325 bar, respectively, in 50 K and 0.20 bar increments. Temperature and pressure were controlled employing Langevin dynamics and Nose-Hoover piston methods [44,45]. The root mean squared deviation data captured from the trajectory of molecular dynamics simulations was used to verify the stability of filament models. The minimized and equilibrated filament structures were used for running all the SMD simulations.

2.2. Steered Molecular Dynamics Simulation Details

The constant velocity SMD simulations for tension, compression and bending were conducted using the NAMD employed approach [43]. The tension and compression test simulations were carried out by fixing one end of the filaments (by applying constraints) and applying pull or push on the center of mass of the terminal G-actin subunits utilizing harmonic spring of fixed spring constant. Previous research indicated that a spring stiffness of 9 kcal/mol/Å^2 is adequate for pulling the F-actin [26]. In the tension and compression test simulations, strain rates of 0.0002, 0.0004, 0.0005, 0.0006, and 0.0008 ps^{-1}were applied. The bending test simulation was carried out by securing both ends of the filament and applying a transverse load at the midpoint. The bending tests were conducted at 0.06, 0.12, 0.14, 0.18, and 0.25 Å/ps displacement velocities. All simulations were conducted at a time step of 0.5 fs. A cutoff distance of 10 Å was used for all nonbonded interactions. Hydrogen bonds (H-bonds) serve an important role in forming and stabilizing protein structures. For all simulations, the evolution of H-bonds was studied using a blend of geometric factors (donor hydrogen distance limit 3.5 Å and donor hydrogen acceptor angle $\leq$30°). In the present study, each simulation was repeated four times. All the stress-strain curves or load-displacement graphs presented here were obtained from averaging results from all four simulations. The error bars in the graphs displaying the mechanical properties of actin filaments represent the standard deviation from the mean (n=4). The initial length (L_0) of the bare F-actin is 31 nm, which was determined by measuring the distance among the centers of mass of the terminal G-actins. The cross-sectional area (A) of the filaments was calculated using the equation $A = \frac{\pi}{4}d^2$ where d is the diameter of the actin filament, $d = 7$ nm.

Recent in vitro studies have shown that a few bound cofilins ($\leq$ 3) are sufficient for efficiently severing the F-actins [29]. The ten subunit F-actin models used in this study captured the molecular-scale details of structural alterations in F-actin caused by cofilin binding. Further, these F-actin models successfully captured the structural characteristics of the fragile regions formed at the cofilin cluster boundary in the filament. Additionally, the F-actin models utilized in this study also captured the transition in mechanical properties of F-actin caused by cofilin. These outcomes demonstrate that the ten subunits F-actin model utilized here is sufficient to study the mechanics of actin filament severing mediated by cofilin.

3. Results and discussion

Previous MD simulation studies conducted to understand the mechanical behavior of the cofilactin filament demonstrated that cofilin binding increases the flexibility of F-actin [46–48]. However, these studies were limited to investigating the mechanical characteristics of actin filaments that are fully decorated with cofilin and did not consider the influence of cofilin cluster boundaries. To fully understand the molecular mechanism of F-actin severing by cofilin, an atomistic model which comprises both cofilin-decorated and bare regions of the F-actin is required. In this work, we built the computational model of partially cofilin decorated actin filament (PCDA filament), containing cofilin decorated segment in the middle with bare actin segments at the pointed end and barbed end side, as shown in Fig. 1b. The role of mechanical loading at different strain rates on the filament severing process is explored using an SMD simulation of PCDA filament. Furthermore, to acquire a comprehensive understanding of the filament severing mechanisms, the deformation behavior of the PCDA filament is compared to the deformation response of bare ADP-F-actin (hereafter referred to as bare F-actin) and FCDA filament using SMD simulations. In addition, the mechanical responses of bare F-actin, PCDA, and FCDA filaments obtained in this investigation are compared to the mechanical properties reported in our previous simulation study on bare ATP-F-actin. The atomistic models of bare F-actin and fully cofilin decorated actin filament (FCDA filament) are shown in Fig. 1a and c. Here, the contacts among neighboring G-actin subunits within a strand (G′ or G) are described as intrastrand (axial) G-actin contacts, and the contacts among neighboring G-actin subunits, one of them from strand G′ and the other from strand G, are described as interstrand (helical) G-actin contacts (Fig. 1).

3.1. Cofilin-induced structural heterogeneity alters the tensile behavior of actin filaments

To investigate the molecular mechanism involved in cofilin-mediated F-actin severing, constant strain SMD simulations for tensile deformation of bare F-actin, FCDA, and PCDA filament models have been performed. The computational setup for tensile simulations where the filaments' barbed (+) ends are fixed and the pointed ends (−) subjected to tensile loading are shown in Fig. 2 a. The tensile stress-strain responses of bare F-actin, FCDA, and PCDA filaments at different strain rates are shown in Fig. 2 b, c, and d, respectively. Each filament model exhibit distinctly different tensile deformation behavior. The stress-strain plot of bare F-actin filament (Fig. 2b) shows four distinctive regions: initial elastic regime (ending with yield point), strain hardening regime, strain-softening regime, and fracture regime.

In comparison, the stress-strain plots for FCDA filament (Fig. 2c) present an initial linear elastic regime followed by yield point, strain-softening regime, and ending in fracture regime with very little or no strain hardening regime. The stress-strain curve for PCDA filament (Fig. 2d), on the other hand, shows a flat plateau-like plastic displacement burst between the yield point and the strain-softening regime, which is followed by the fracture regime. The variation in tensile strength, fracture strain, and elastic modulus of the three filament models for different strain rates is shown in Fig. 2 e, f, and g. Between the three filament models for all strain rates, the FCDA filament model has the highest tensile strength and elastic modulus. In contrast, the PCDA filament model has the lowest tensile strength and elastic modulus. Further, Fig. 2 (f) indicates that the FCDA filament has the highest, and the PCDA filament model has the lowest fracture strain. These results are consistent with a previous in vitro study in which a microfluidic chamber-based fluid flow setup was utilized to apply tensile load on cofilin decorated F-actins [49] suggesting that small cofilin clusters efficiently sever F-actin. However, the large cofilin clusters lead to merging and a significant reduction in the number of cluster boundaries and chances for filament severing. The tensile strength and elastic modulus values for all the three filament models were

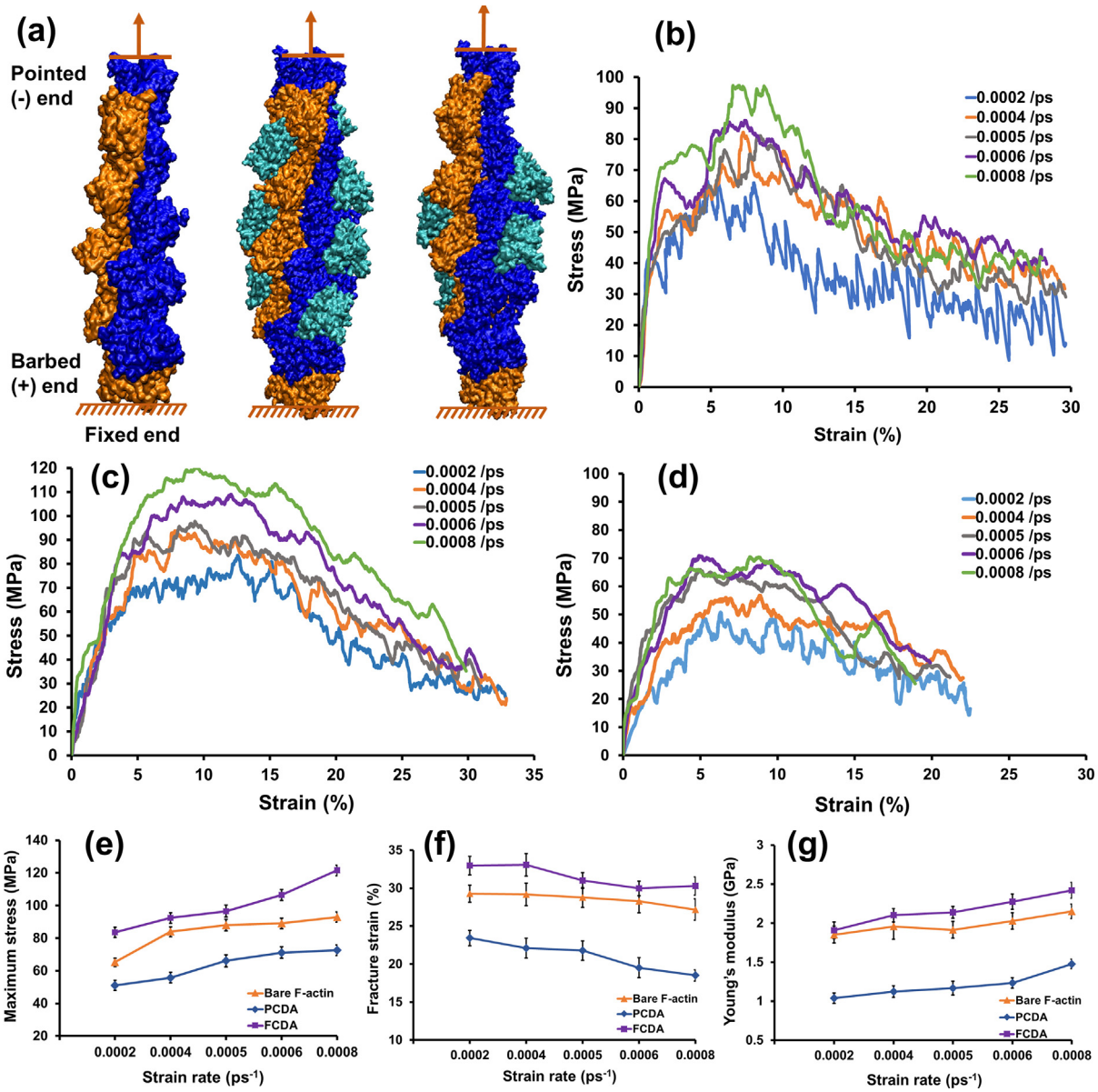

Fig. 2. Tensile strength, fracture strain, and Young's modulus as a function of strain rate. (a) Computational setup representing atomic structures of bare F-actin, FCDA, and PCDA filaments with the barbed (+) end fixed and the free end (pointed (-) end subjected to tensile load. (b-d) The stress-strain graphs of bare F-actin (b), FCDA (c), and PCDA (d) filaments at various strain rates. (e-g) Plots demonstrating the variation in tensile strength (e), fracture strain (f), and Young's modulus (g) of three filament models as a function of strain rate.

observed to increase with the increase in strain rate. However, the fracture strain of all filament models decreased as the strain rate increased, demonstrating that higher stress levels were linked to reduced filament plasticity.

To understand the basis of variability in the mechanical properties of bare F-actin, FCDA, and PCDA filament, correlating their deformation behavior with their structural differences is essential. In bare F-actin, the wavy stress-strain response sharply increases to its elastic limit in a strain range of 0% to 4% strain, and then it starts dropping until it approaches the Yield point at a 4-5% strain. Further, in the strain hardening regime, the F-actin continues to elongate with increasing stress to its maximum limit at approximately 8% strain. Subsequently, stress starts dropping slowly in the strain-softening regime until it reaches a 20% strain. In the fracture regime, the bare F-actin continues to elongate beyond 20% strain, nearly at constant mean stress. The fracture regime indicated that bare F-actin breaks nearly under constant stress conditions and is consistent with a previous experimental investigation revealing that F-actin begins to rupture and flow at approximately 20% strain [50]. We observed that the geometrical features of G-actin subunits and their structural organization in a double-stranded helix of the filament influence the deformation behavior of bare F-actin. In bare F-actin, conformational locking between G-actins along the helical strand primarily consists of electrostatic and hydrophilic interactions [51].

Fig. 3 displays the evolution of the deformation profile of three filament models in their undeformed state (0% strain), at the yield point (4-6% strain) and strain corresponding to tensile strength (10% strain), at the end of the strain hardening phase (13-15% strain), and the fracture stage. Studying the deformation simulation trajectories (Fig. 3a) in conjunction with the stress-strain plot reveals that the initial deformation of bare F-actin is dominated by intrastrand G-actin contacts stretching (axial interaction). Therefore, the G-actin subunits in a strand begin to separate when

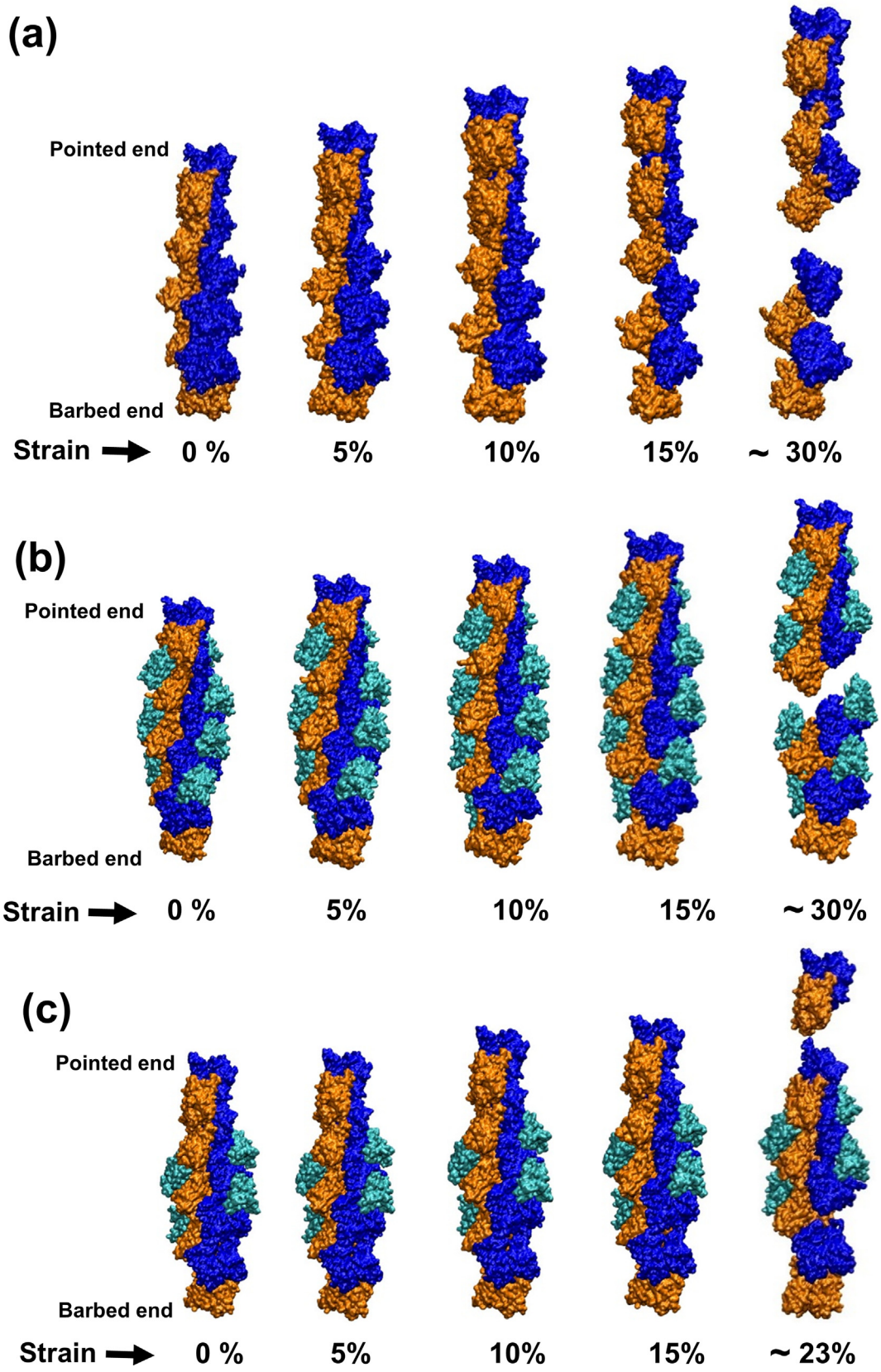

Fig. 3. Snapshots showing the tensile deformation mechanism and failure modes of three filament models. Atomic snapshots display the trajectory of the deformation of three filament models from their initial state (0% strain), the yield point (4-6%), and the end of the strain hardening phase (12-15%), and the fracture point. The snapshots 3a, 3b, and 3c also display failure modes of bare F-actin, PCDA, and FCDA filament, respectively (acquired at 0.0006 /ps at strain rate). The failure mechanism seen during tensile deformation of PCDA filament differs markedly from those observed in bare F-actin and FCDA filament models.

stretched, and they disassociate entirely at 10–12 % strain. Fig. 4 (a-b) displays the variation in the number of interfacial hydrogen bonds as a function of strain for the bare F-actin model during the tensile deformation at different strain rates. The tensile stress in bare F-actin promotes uncoiling and sliding of the conformational locking at intrastrand G-actin interfaces. As a result, the number of interfacial H-bonds at intrastrand interfaces drops rapidly in the strain range corresponding to the yield point, strain hardening regime, and approaches zero at the end of the strain hardening regime (13–15% strain), as shown in Fig. 4a. Also, we observed that when tensile strain reaches the yield point, shear deformation at interstrand G-actin interfaces becomes active, resulting in a specific pattern of hydrogen bond variation as a function of strain, as shown in Fig. 4b. Therefore, the number of interfacial H-bonds at interstrand G-actin interfaces remains relatively constant up to the yield point and starts decreasing gradually beyond the yield point.

The rapid drop in the number of H-bonds in bare F-actin at intrastrand G-actin interfaces up to the strain corresponding to tensile strength shows that intrastrand interaction plays a vital role in defining the elastic modulus as well as the overall deformation behavior of the bare F-actin. The deformation trajectories indicate that the strain hardening regime observed in bare F-actin is likely due to sliding and stretching of the conformational lock at intrastrand G-actin interfaces combined with shear deformation at the interstrand G-actin interfaces, as shown in supplementary

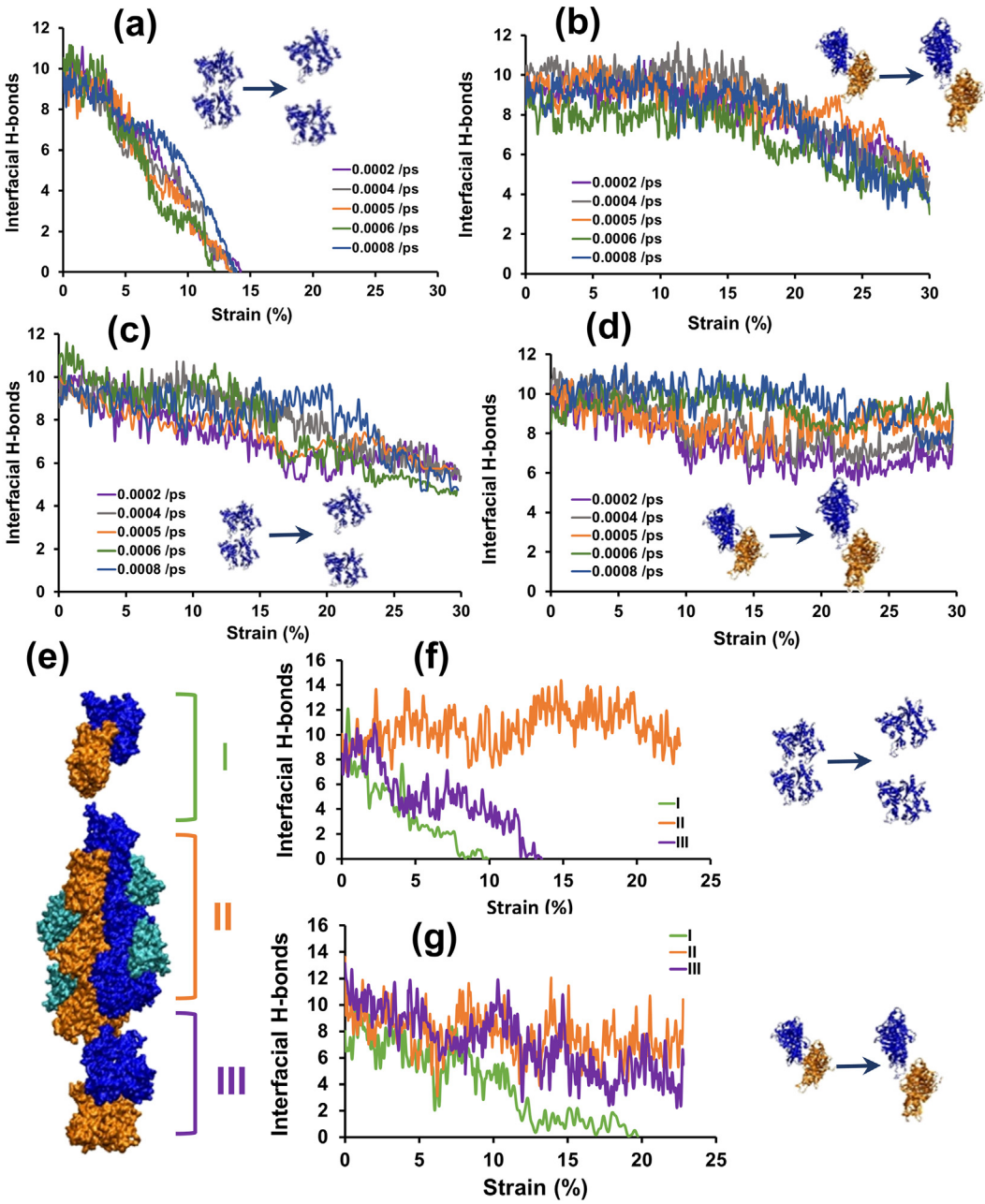

Fig. 4. Variation in hydrogen bonds (H-bonds) for three filament models during tensile deformation at different strain rates. (a-b) The changes in intrastrand and interstrand G-actin interfacial H-bonds in the bare F-actin response to applied strain are shown in graphs a and b. (c-d) Graphs c and d represent the variation in intrastrand and interstrand G-actin interfacial H-bonds in the FCDA filament as a function of applied strain. (e) The segments of the PCDA filament starting from the pointed end are designated as regions I, II, and III. (f-g) The changes in intrastrand and interstrand G-actin interfacial hydrogen bonds in regions I, II, and III of PCDA filament as a function strain are shown in graphs f and g.

Fig. 1 a-b. The stress-strain plot for the FCDA filament shows that cofilin binding to F-actin increased its tensile strength and elongation at break. It can be seen in Fig. 3b that the cofilin binding to the actin filament enables it to interact simultaneously with the two adjacent G-actin subunits along the respective helical strands. Upon analysis of the deformation trajectory of FCDA filament, it is found that, during tensile loading, the interconnectivity between adjacent G-actins via cofilin facilitates the load transmission between them. Therefore, the filament stretching also resulted in tensile deformation of cofilin. Fig. 4 (c-d) displays the variation in the number of interfacial hydrogen bonds with strain for the FCDA filament model during the tensile deformation at different strain rates. The number of H-bonds at intrastrand and interstrand G-actin interfaces in FCDA filament drops slowly in the strain range corresponding to the yield point (6 % strain) and beyond. This observation indicates that cofilin bonding between two adjacent G-actins restricts the tensile deformation at intrastrand G-actin interfaces and shear deformation at interstrand G-actin interfaces, resulting in higher FCDA filament tensile strength. It appears that the cofilin works as a bridge that stabilizes the intrastrand and interstrand contact between adjacent G-actin subunits. This finding is consistent with previous research claiming that cofilin-saturated actin filaments are not easily fragmented [18].

Fig. 3 c displays the snapshots of the PCDA filament's failure mode (rupture) observed at the end of the fracture regime during tensile loading (at ~23% strain). Correlating the simulation trajectory of PCDA filament with its stress-strain behavior, it is observed that the bare F-actin segments and cofilin decorated actin segments endure an equivalent magnitude of deformations at all strain rates up to the yield point (5% strain). Based on these observations, it can be concluded that both the segments in the PCDA filament are equally contributing to carrying the load up to the yield point, providing an equivalent amount of resistance to deformation. In subsequent stress-strain regimes, as stress increases, the cofilin segment boundaries start uncoiling and stretching considerably, resulting in significant plastic deformation. In contrast, minor deformation is observed in the cofilin decorated region beyond 7-8% strain. The structure of cofilin decorated actin segments differs from bare actin filaments [32,52]; consequently, it was hypothesized that structural discontinuities at the boundaries between cofilin-bound and bare regions of the filament produce mechanically weak sites [52]. The two cofilin cluster boundaries are not structurally identical. It has been observed that the actin filament severs at a faster rate at the pointed end side of the cluster than on the barbed end side [29,30]. The comparable results observed here show that the segment boundary at the pointed end deforms more rapidly than the segment boundary at the barbed end in PCDA filament, resulting in filament severing at the cluster boundary towards the pointed end. Cofilin disrupts longitudinal contacts between F-actin subunits by altering the structure of G-actin subunits [23]. Therefore, the longitudinal heterogeneous distribution of deformation response in the PCDA filament seen here can be likely due to the weak connectivity between the bare F-actin segment and the cofilin decorated segment towards the pointed end.

For a deeper understanding, it is necessary to analyze the deformation response of each segment of the PCDA filament. In doing so, the bare F-actin segment towards the pointed end, cofilin decorated segment at the middle, and bare F-actin segment towards the barbed end are designated as regions I, II, and III, respectively, as shown in the Fig. 4e. The variation in the number of H-bonds in the region I, II, and III in PCDA filament has been investigated to thoroughly understand the mechanisms behind the significant differences in dissociation rate at the pointed end side compared to the barbed end side of the cluster boundary. Fig. 4 f, g depicts the variation in the number of hydrogen bonds at intrastrand and interstrand G-actin interfaces in regions I, II, and III as a function of applied strain. The intrastrand G-actin-G-actin contact at the segment boundary near the pointed end (regions I) stretched under tensile load and dissociated entirely at 8-9 % strain; however, at the interstrand interface, G-actin subunits remained in contact until the filament ruptures at 20-23 % strain. As a result, hydrogen bond breakage at intrastrand G-actin interfaces at the segment boundary in region I occur rapidly; consequently, the number of interfacial hydrogen bonds approaches zero at approximately 9 % strain. We found that the cofilin-mediated change in the configuration of G-actins disrupted their D-loop contacts with adjacent G-actins at the cluster's boundary toward the pointed end. Observing the deformation trajectory of PCDA, we found that although the intrastrand G-actin contacts at the cofilin cluster boundary near the pointed end exhibited tensile deformations, the D-loop of the G-actins appeared to have undergone negligible stretching deformations. Therefore cofilin-mediated alterations in G-actin D-loop interactions with their adjacent intrastrand subunits are a likely contributor to the formation of fragile cluster boundaries and the overall stiffness of filaments. In the subsequent section, these observations have been discussed in detail. The tensile strain also causes G-actin subunits to slide at interstrand interfaces; as a result, the number of hydrogen bonds at the interstrand G-actin interface at the segment boundary near the pointed end began to decline gradually with the strain and approaches zero at approximately 20-23 % strain (rupture point). The trends remain relatively similar at the segment boundary near the barbed end (in region III) of PCDA filament with a slightly different deformation behavior. The tensile loading extends the intrastrand G-actin interfaces at the segment boundary towards the barbed end, causing complete separation of neighboring G-actins in the strand at 15-16 % strain. Accordingly, the H-bonds at the intrastrand G-actin interface in region III approach zero within 0-16% strain. The tensile deformation of filament also caused the sliding of G-actin subunits at the interstrand interface. Therefore, the number of H-bonds at the interstrand G-actin interfaces at the segment boundary towards the barbed end remained relatively constant with slight fluctuations. Hydrogen bond analysis in regions I and III show that intra-strand and interstrand G-actin interactions are more stable at segment boundaries towards the filament's barbed end than at the pointed end. Region II represents the cofilin decorated segment of the PCDA filament. Region II of the filament deforms slightly up to 10 % strain; however, minor deformation is observed under tensile loading in region II of the filament beyond 10 % strain. Therefore, the number of interfacial H-bonds at the intrastrand and interstrand G-actin in region II remains nearly constant, with an applied strain ranging from 0 to 23%. The deformation and rupture behavior of the PDAC filament is consistent with prior experimental studies suggesting that the filament severing is biased and occurs on the pointed end side of cofilin clusters than on the barbed end side. These findings demonstrate that we have created atomistic models of cofilactin filaments that accurately mimic the severing behavior observed in previous experimental studies. Understanding the basic structure of actin filament subunits and cofilin-linked structural alterations is also crucial for investigating the molecular mechanisms of cofilin-mediated F-actin severing. Therefore, our simulation has also captured the change in the structure of F-actin subunits mediated by cofilin, implying that the severing of PCDA filaments on the pointed end side of cofilin clusters is connected with structural discontinuities caused by cofilin binding.

3.1.1. The ADF/Cofilin Interactions Tilts and Disrupts the D-Loop of G-actin Subunits

The G-actin molecule is broadly divided into two domains: the inner domain (ID) consists of subdomains (SD) 3 and 4, and the outer domain (OD) consists of subdomains (SD) 1 and 2 (Fig. 5a).

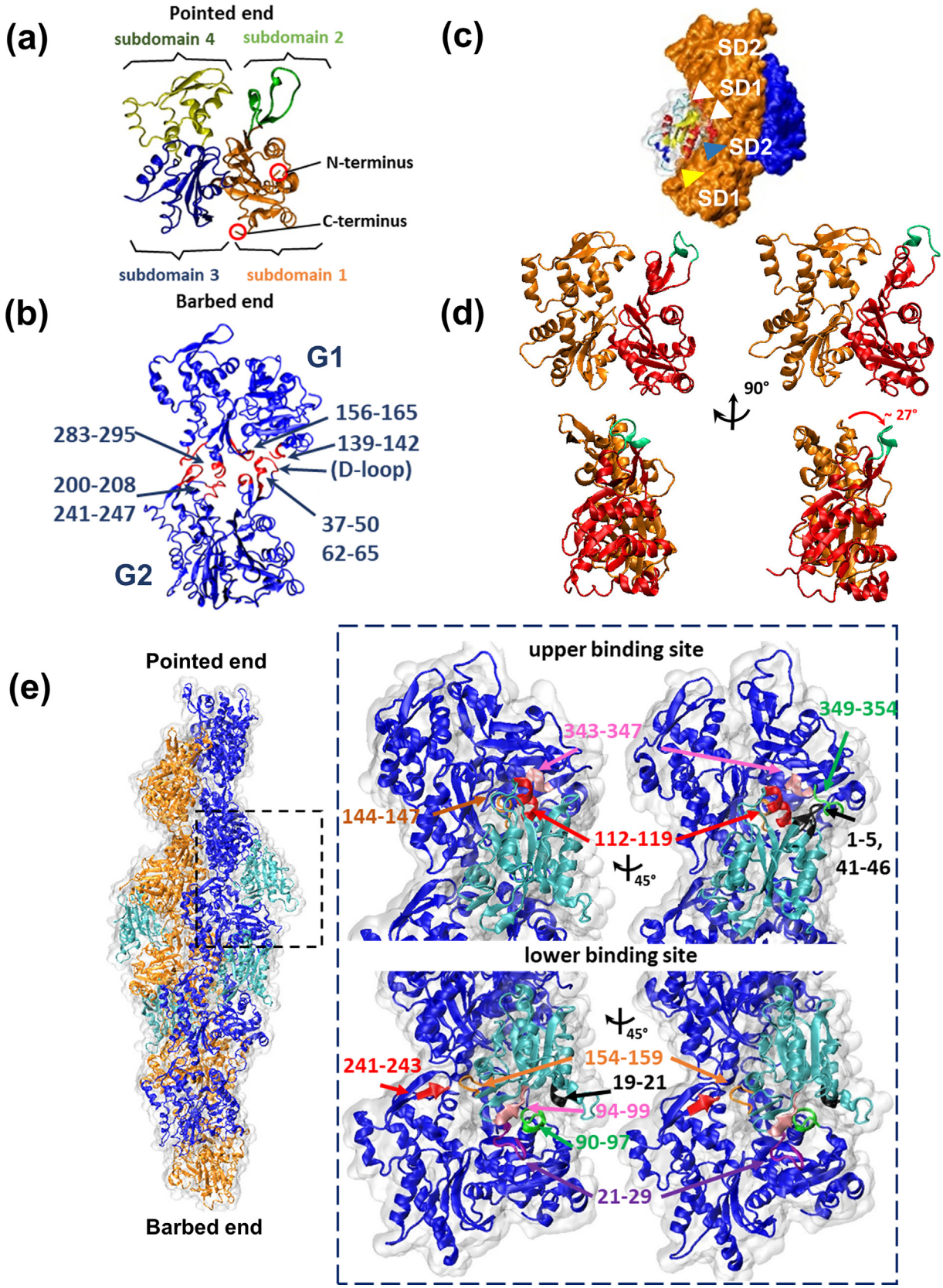

Fig. 5. The classical view of G-actin subunit structure, intrastrand G-actin contact interface, and Cofilin-G-actin interactions. (a) The domain structure of G-actin. (b) Intrastrand G-actins interactions and contact-forming residues are highlighted in red. (c) When a cofilin monomer binds to F-actin, the α4-helix has a steric clashing with SD1 and SD2 of G-actins (as shown by white and blue arrowheads), whereas the α1-helix clashes with SD1 of G-actin (yellow arrowheads). (d) Comparison between filaments G-actin structure in its native state (on the left) and when bound with cofilin (on the right). D-loop highlighted the green. The steric clashes are resolved by rotating the outer domain of G-actin by roughly 27° (red arrow). (e) Cofilin makes multiple contacts with two adjacent G-actin subunits described as the upper and lower binding sites.

Subdomains 1, 3, and 4 have well-defined hydrophobic cores and act as rigid, independent units in a filament. Subdomain 2 has a D-loop between residues 40 (His) and 48. (Gly). Conformational organization and nonbonded interactions mediate stable intrastrand contacts between G-actin subunits [51].

Fig. 5b illustrates these features; the conformational projections of G-actin subunit G1 (residues 283-295, 156-165) enclosed by G2-subunit residues 37-50, 62-65, 200-208, and 241-247. Furthermore, Subunit G2's D-loop (40-48) extends toward subunit G1's upper cavity between SD 1 (residue 139-142) and 3 (residue 159-165). SD 4 of G2 is also in close contact with G1's domain 3. Cofilin's interaction with G-actins in a filament can be divided into two distinct regions: cofilin binding to G-actin towards the pointed end (upper binding site), and cofilin binding to G-actin towards the barbed end (lower binding site), as shown in the Fig. 5 c, e. The upper binding site comprises two contacts: G-actin residues 144–147 and 343–347 interact with cofilin residues 112–119 near the α4-helix. While G-actin's C-terminal residues (349–354) also make extensive contact with the loop 41–46 and the N terminus of cofilin (residues 1-5), as shown in Fig. 5e. Cofilin's lower binding site also has two distinct contacts. The first contact is created between the small loop of cofilin (residues 154–159) and actin residues 241–243 in Subdomain 4 (SD4) (Fig. 5e). The second contact involves cofilin residues 94–99 interaction with actin residues 21–29 and 90–97 in Subdomain 1 (SD1). Cofilin residues 19–21 in the α1-helix also interact with actin residues 90–97. Cofilin binding to F-actin results in two steric clashes: the α4-helix of cofilin molecule and the SD1 of one G-actin and SD2 of adjacent intrastrand G-actin (Fig. 5c, white and blue arrowheads) and the other between the α1 helix of cofilin and the SD1 of G-actin (Fig. 5c, yellow arrowheads). To prevent these clashes, the G-actin subunits in contact with cofilin adopt a new configuration wherein each subunit's OD rotates by approximately ∼ 27° towards the opposite helical strand (Fig. 5d). However, the intrastrand interaction between adjacent G-actin subunits mediated by ID remains unaffected. The rotation of the outer domain of G-actin causes a change in intrastrand G-actin contacts. We observed that the rotation of the outer domain of G-actin subunits resulted in a significant structural defect in F-actin. We suggest a plausible mechanistic model explaining how cofilin binding to F-actin can trigger its severing at the cofilin cluster boundary towards the pointed end side.

3.1.2. The structural mechanism of F-actin severing by ADF/cofilin

When cofilin attaches to F-actin, G-actins in contact with cofilin change their orientations and conformation. The schematic model of bare F-actin and PCDA filaments shown here provides a structural explanation for how the severing process can be more biased toward the pointed end side of the cofilin cluster (Fig. 6). The G-actin structure is analogous to interlocking pieces, with all four subdomains resembling rounded jigsaw tabs (jambs) and clefts between subdomains representing blanks. As illustrated in Fig. 6a, bare F-actin is an assembly of G-actins where the projections of subdomain 3 of one G-actin fit in the cleft formed between subdomains 2 and 4 of successive G-actin toward the barbed end. While the projections of subdomain 2 of successive G-actin also fit in the cleft formed between subdomains 1 and 3. Therefore, the intrastrand contact formed between G-actins by conformational locking between respective subdomains is portrayed here as interlocking jigsaw puzzle pieces (Fig. 6a). Fig. 6a-b represent a schematic of bare F-actin's single-stranded and double-stranded structures as an untwisted helix. The schematic of the PCDA filament shown in Fig. 6c here is based on three observations: (1) Cofilin binding rotates the outer domain of G-actins. This conformational shift weakens the intrastrand G-actin contacts. (2) Filament severing occurs only where the intrastrand contact on both strands has been disrupted. (3) Cofilin acts as a strong bridge between two adjacent G-actin.

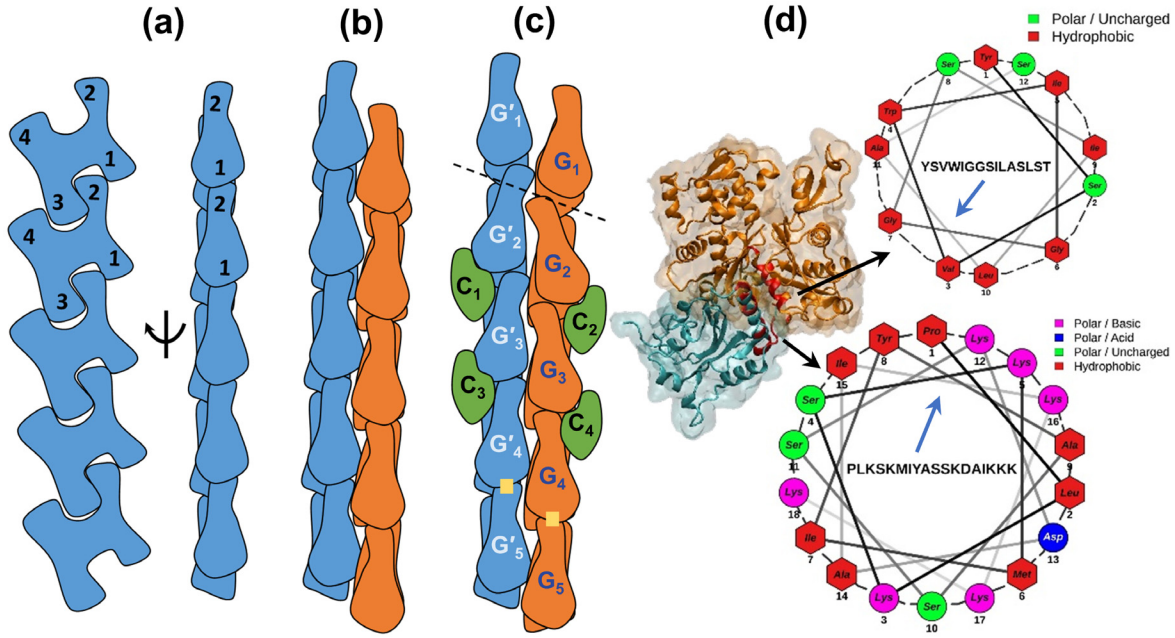

Fig. 6. F-actin severing model (a) The single-stranded structure of bare F-actin (blue). Intrastrand G-actin interaction created by conformational locking between respective subdomains (SD 1, 2, 3, and 4) of G-actin is presented here as interlocking jigsaw puzzle pieces. (b) A double-stranded structure of bare F-actin (blue and orange) is represented as an uncoiled helix. (c) PCDA filament structure with cofilin cluster at the middle (green) displaying naming conventions. The G-actin subunits directly in contact with cofilin adopt the tilted conformation, which disrupts the contacts with the axial neighbor, forming a fragile zone at the cluster boundary toward the pointed end (black dashed line). Since cofilin act as a strong cross-bridge between adjacent G-actins, the cluster segment, and barbed end side bare F-actin segment remain stable. Intact intrastrand G-actin contacts at the barbed end are represented as yellow squares. (d) Hydrophobically active cofilin and G-actin contact region (red). Conformations and helical wheel representations of α-helix of G-actin (residues 337-348) and α4-helix of the cofilin. The blue arrows indicate the hydrophobic face.

Fig. 6c shows a schematic of a PCDA filament that highlights the structural changes caused by the cofilin cluster. All G-actin subunits that come into contact with cofilin adopt a tilted conformation, as seen in Fig. 6c. The rotation of the outer domain of G′2 and G2 subunits terminates the D-loop interactions with the longitudinal neighbor G′1 and G1 subunits (dashed black line). Similarly, rotation of the outer domains of G′3 and G3 subunits compromises their intrastrand connections with neighbors G′2 and G2 subunits. However, the neighboring G-actins at the barbed end side of the cluster (G′4 and G4) do not tilt. Cofilin binding compensates for compromised intrastrand interactions between G′2-G′3 and G2-G3 subunits. Yellow squares indicate intact D-loop interaction with adjacent G-actins. Because intrastrand conformational locking is disrupted at the pointed end cofilin cluster boundary, it becomes a possible severing site. The plausible mechanistic hypothesis explains how F-actin severs at the pointed end of a cofilin cluster. It also helps to understand why the binding of just one cofilin molecule is insufficient for efficiently severing F-actin [32]. The plausible F-actin severing model shown here is based on prior and current findings. We anticipate that the F-actin severing model discussed here will aid a thorough understanding of ADF/cofilin functions in actin cytoskeleton dynamics.

The cofilins structure consists of six β-sheets enclosed by five α-helices. The first five residues in the N-terminus of cofilin play a critical role in its binding to G-actin. Removing the first five residues in the N-terminus of cofilin inhibits its binding to G-actin and F-actin [53,54]. Cofilin's α4-helix establishes multiple vital contacts with G-actin [55]. We observed that the amino acid sequence in the α-helix of G-actin (residues 337-348) shows distinct segmentation of hydrophobic and polar residues on two opposite faces of the α-helix. The distinct segmentation of hydrophobic and polar residues on opposite faces of the α-helix is a characteristic feature of the amphipathic helix [56]. We noticed that the α-helix of G-actin orients its hydrophobic face toward the N-terminus and α4-helix of the cofilin. Generally, amphipathic helices (AHs) are composed of a series of hydrophobic amino acids distributed with polar residues in between, allowing the helix to exhibit two faces with opposing chemical properties: a polar face and a hydrophobic face [57]. Amphipathic α-helices are essential in early peptide and protein segment folding [58,59]. As illustrated in Fig. 6d, the cofilin α4-helix makes multiple interactions with SD1 of G-actin, including α-helix. The first five hydrophobic residues forming the cofilin's N-terminus also create multiple close interactions with the α-helix of G-actin, making the cofilin and G-actin contact region hydrophobically active. Hydrophobic interactions are critical for stabilizing the binding structures of single proteins, multiprotein complexes, and protein-ligand systems [60–62]. Therefore hydrophobic interactions between α-helix of G-actin and α4-helix plus the N-terminus of the cofilin may have a critical role in the rotation of the outer domain of G-actin and disruption of longitudinal G-actin connection, causing actin filament severing.

3.2. Actin filaments partially decorated with cofilin have lower compressive strength than actin filaments fully decorated with cofilin.

Actin filament's structural deformations, such as buckling during compressive loads caused by contractile myosin proteins, stimulate the filament fracture and can promote the filament severing process by ADF/cofilin [48]. Furthermore, the structural alterations in actin filaments induced by cofilin binding reduce the force required for its buckling and make actin bundles and networks unstable, speeding up actin turnover in cells [63]. Hence for identifying the molecular basis of actin filament severing, a quantitative understanding of actin filament deformation behavior under compressive load is essential. In this study, constant velocity SMD simulations have been employed to explore the deformation behavior of the PCDA and FCDA filaments under compressive loading in a computational setting. The central objective of the simulations is to gauge the influence of cofilin binding on the mechanical properties of the F-actin under compressive load and understand the significance of the cofilin cluster boundary on the filament severing process.

The compression simulation setups in which the standard SMD protocol has been used to apply compressive forces to the PCDA and FCDA filaments at a constant strain rate are shown in Fig. 7 a-b. Fig. 7 a-b also displays the snapshots of the deformation profile of the PCDA and FCDA filament models under compression (the snapshots acquired for 0.0006/ps strain rate). Considering the short length of filaments, we used the general stress equation (Stress = Force/Cross-sectional area) to calculate compressive stresses in the filaments. The stress-strain curves of the PCDA filament and FCDA filament under compressive loading obtained by SMD simulation are shown in Fig. 7 c-d. The ends of the curves shown here indicate how far the simulation was run and should not be considered a failure point. It can be seen that the compressive strength of both filament models' increased as the strain rate increased.

The stress-strain curve for PCDA filament showed a consistent behavior for all the strain rates; a linear elastic response in the initial loading stage (8% strain), followed by moderate nonlinear behavior with a minor stress drop at 10–12% strain, and then followed by strain hardening. FCDA filament, on the other hand, has a slightly different deformation behavior. It appears that the FCDA filament experienced no stress drop after the initial linear elastic response (8% strain) and that they displayed strain hardening after the yielding point (12% strain). Our previous work [26] detected that a bare F-actin begins to buckle at about 15% compressive strain, attaining ultimate compressive stress of 120.5 MPa. Then stress begins to decrease with increasing compression [26]. However, the PCDA and FCDA filament stress-strain curves exhibit a gradual and continuous increase in compressive stress with increasing strain. The stress-strain curve for PCDA filaments at a similar strain rate displays the compressive stress of 114.6 MPa, achieved at 15% compressive strain and with no visible filament buckling. However, using the identical simulation parameters, FCDA filament was found to endure compressive stress of 163.5 MPa at roughly 15% compressive strain, which is substantially greater than PCDA filament for equivalent strain. The initial linear response in PCDA and FCDA filament stress-strain curves shows a significant slope difference. The difference in slopes represents the difference in compressive modulus of PCDA and FCDA filaments. Considering the stress-strain plot up to 10% strain, the obtained average compressive modulus of PCDA and FCDA filament are 1.42 ± 0.2 GPa and 2.01 ± 0.1 GPa, respectively. Comparing the 1.62 ± 0.18 GPa compressive modulus of bare F-actin obtained from our previous study under similar stimulation settings, it can be seen that the partial cofilin decoration of the filament led to a slight reduction in compressive modulus in PCDA filament. However, complete cofilin decoration of the filament resulted in a substantial increase in compressive modulus in the FCDA filament.

In order to understand the basis of variability in the compressive response of PCDA and FCDA filament, it is essential to correlate their stress-strain plots with their deformation profiles. It is found that in the strain range of 0 to 8% total strain, the strain distribution in the PCDA filament is non-uniform along its length. Analysis of the PCDA filament deformation trajectory reveals that during compressive loading, in the initial 0 to 8 % strain range, substantial nonlinear sliding deformation of the G-actin interfaces occurs at the pointed end side of cofilin clusters (as indicated by the green box in Fig. 7a. As a result, the PCDA filament's initial 0–8% strain is primarily localized at the cofilin cluster boundary at the pointed

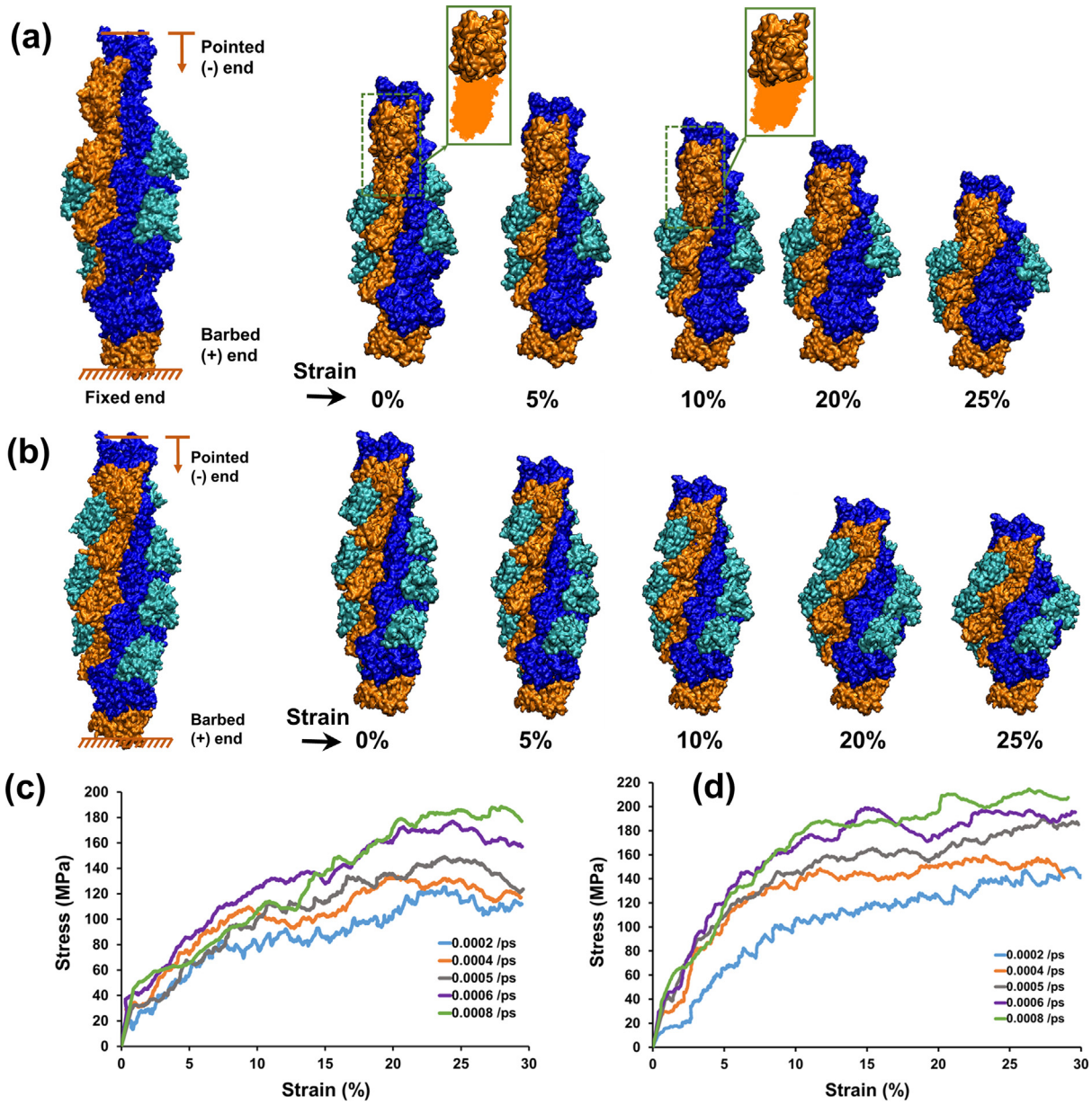

Fig. 7. Images showing the deformation profile and compressive strength of filament models as a function of strain rate. (a-b) The atomic structure of a PCDA and FCDA filament with the barbed end fixed and the pointed end subjected to a compressive force, with visualization of compressive deformations. Considerable sliding deformation of G-actin interfaces occurs at the pointed end side of cofilin clusters during the initial 0 to 8% strain range (green squares). (c-d) The strain-rate sensitive compressive deformation response of PCDA (c) and FCDA (d) filaments.

end with a minor deformation of the cofilin cluster segment. The non-uniform longitudinal strain in the PCDA filament could have resulted from the structural discontinuities caused by cofilin binding, as discussed in section 3.1.1. Beyond 8% strain in the PCDA filament, the compressive deformation in the bare and cofilin cluster segment appears consistent. The altered compressive deformation of G-actin interfaces at cofilin cluster boundaries towards the pointed end plays a crucial role in decreased compressive strength of PCDA filaments. The FCDA filament model consists of actin filament fully decorated with cofilin; therefore, cofilin cluster boundaries formed by the cofilin binding do not exist in its structure. During the compression test, we observed that the strain in the FCDA filament appears to be consistent along its length. It is also observed that the compressive force in the filaments produces considerable compression (compressive deformation) of the cofilin and G-actin subunits. Supplementary Fig. 2 a-f illustrates these characteristics by displaying the change in the number of hydrogen bonds in PCDA and FCDA filaments as a function of percentage compressive strain. It can be seen that the total H-bonds in PCDA and FCDA filaments and their G-actin and cofilin subunits reduce as compressive strain increases. Since the compressive deformation of individual subunits demands the simultaneous breaking of multiple hydrogen bonds, FCDA filament exhibits a stiffer response in compression. However, the presence of partial cofilin decorated regions in the filament slightly reduced the compressive modulus of the PCDA filament in comparison to the previously reported compressive modulus of bare F-actin.

3.3. Partially cofilin-decorated actin filaments are more flexible in bending than fully cofilin-decorated actin filaments

Actin filaments withstand various stresses in order to maintain cell shape and support motor proteins in generating force for cell movement and shape changes [1,64]. Actin filament's resistance

to the applied load can cause them to bend and buckle; hence the resistance to bending of an actin filament is a critical quantity to measure [27]. Cofilin-mediated changes in actin filament structure can modify its local resistance to bending. It has been reported that cofilin binding reduces the flexural rigidity and persistence length of actin filaments, making them more flexible than bare actin filaments [24,65]. It has also been shown that cofilin-mediated actin filament severing activity is interrelated with its effect on actin filament flexibility [66]. Furthermore, few previous in vitro studies have revealed that small cofilin clusters (consisting of less than three cofilin subunits) can sever actin filaments, with no observable severing dependence on cluster size [29,67]. A question then arises, what is the molecular mechanism by which cofilin increases the bending flexibility of F-actin. There are, however, two possible mechanisms for the increased bending flexibility of F-actin: (1) the cofilin-decorated region of the actin filament becomes more flexible in bending, resulting in an overall increase in bending flexibility of F-actin; or (2) the fragile regions formed at cofilin cluster boundaries induce an overall increase in bending flexibility of F-actin.

The mechanical features of biomolecular structures, such as bending rigidities, have been effectively investigated using steered molecular dynamics (SMD) simulations [68,69]. Therefore, here, SMD simulation has been utilized to study and analyze the influence of cofilin clusters on the bending mechanics of actin filaments. The three-point bending experiment has been one of the basic procedures for conducting bending tests to determine the biopolymers' flexural rigidity or bending stiffness. In the computational setup, we applied the harmonic constraint on the terminal G-actins to fix both ends of the PCDA and FCDA filaments, as shown in Fig. 8a. Then, the midpoint of the filaments was chosen to apply a force perpendicular to the longitudinal axis of the filaments up to a deflection of about 7 nm. The setup shown here closely resembles F-actin bending deformation in a cell cytoskeleton environment. The force-displacement curves for PCDA and FCDA filaments are presented in Fig. 8 c and d. It can be seen that the force-displacement curve for FCDA filament initially exhibits linear elastic behavior up to approximately 2.5 nm displacement. This is further followed by a nonlinear flat region demonstrating plastic deformation, where the mean force remains almost constant as displacement increases. The force-displacement curve for PCDA filament follows a similar trend; however, after 5 nm displacement, the force decreases with increasing displacement. For all pulling velocities, comparisons of the force-displacement curves of both the filament models show that the maximum bending forces for the PCDA filament are significantly lower than those for the FCDA filament. Also, the force required for 2.5 nm displacement for FCDA at all velocities is approximately 20-25% more than for PCDA, indi-

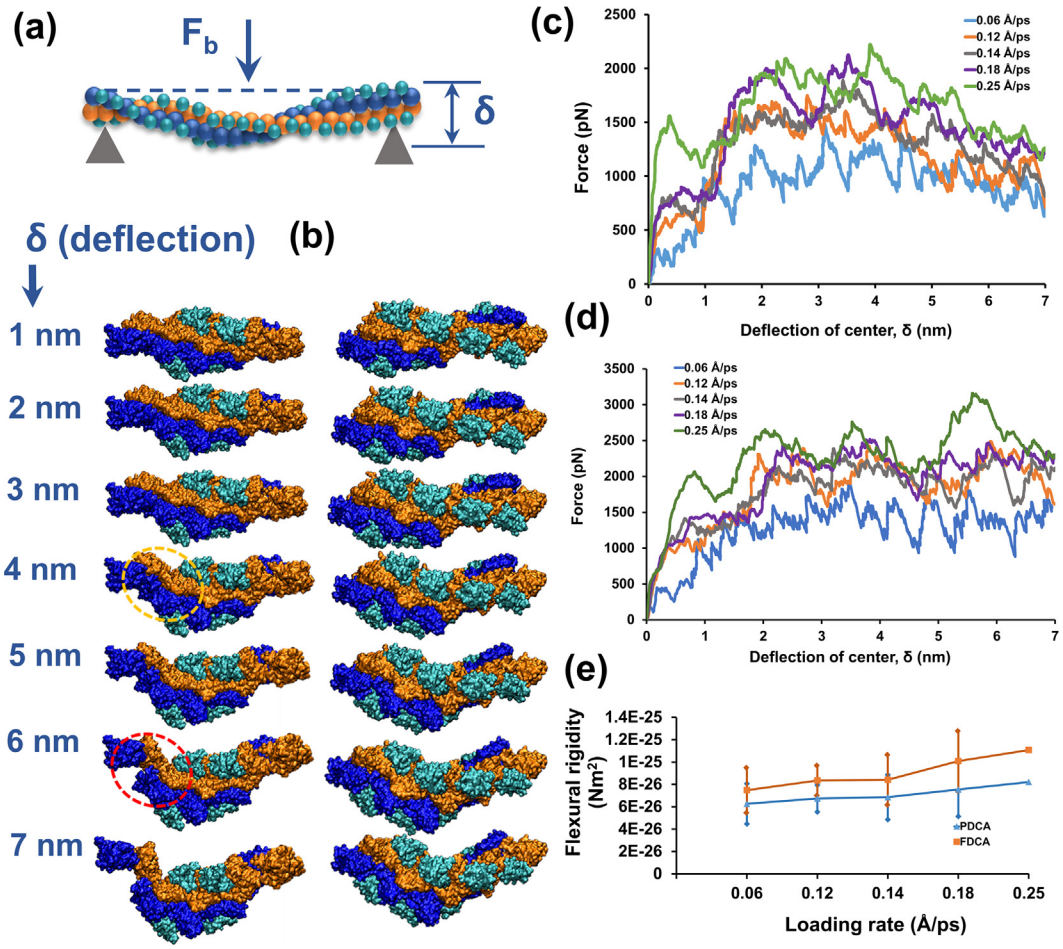

Fig. 8. Schematic illustration of the bending test with deformation behavior documented at various loading rates. (a) Graphical illustration of the computational bending test setup. The filament model is placed horizontally, with ends fixed and subjected to point load at the center. (b) Images show bending deformation of PCDA and FCDA filaments as deflection increases. The PCDA filament begins to break (yellow circle) on the tension side between the tension and compression sides, and significant damage occurs at approximately 6 nm displacement (red circle). (c-d) A force-displacement curve demonstrates the bending response of PCDA (c) and FCDA (d) filaments. (e) Flexural rigidity is plotted as a function of loading rate.

cating that the bending stiffness of FCDA filament is significantly higher than PCDA filament. We also examined the evolution of both filament configurations as a function of bending deflection. Fig. 8b represents how the bending load on both the filaments (PCDA and FCDA) resulted in a concave curvature-shaped structural deformation. Bending induces compressive stress in the top region of the filaments as the G-actin and cofilin subunits in that region are compressed together. Bending also induces the tensile stress in the lower face of the filaments where G-actin and cofilin subunits are pulled apart. As shown in Fig. 8b, as the bending deformation increased within the 0- 2.5 nm displacement range, no visible change in the FCDA and PCDA filament subunit interfaces has been observed. The plastic flow region of the force-displacement curve in both filaments represents bending deformation beyond 2.5 nm displacement, suggesting the substantial structural deformation in the PCDA and FCDA filament and their subunit interfaces beyond this point. The bending deformations create compression and tension on the longitudinally opposite sides of the filaments. Observable bending deformation in the PCDA filament has been observed at approximately 4 nm displacement, suggesting fracture initiation at the cluster boundary towards the pointed end. The gradual decrease in the force required for bending in the PCDA filament after the occurrence of the first fracture (5 nm) indicates that the filament is no longer capable of supporting bending inducing load and is on the verge of failure. Consequently, it can be seen that as bending progresses at approximately 7 nm displacement, the PCDA filament almost ruptured at the cluster boundary towards the pointed end. In contrast, no noticeable incidence of bending fracture has been observed in FCDA filament in the bending deflection range of 0-7 nm, suggesting that fully cofilin decoration improves the bending strength of the actin filaments. Continuous decrease in the total number of hydrogen bonds in PCDA and FCDA filament beyond 2.5 nm of displacement indicates distortion of G-actin interfaces as bending progress (Supplementary Fig. 3 a-b).

One of the approaches to characterize the actin filaments' bending flexibility is to measure its flexural rigidity and persistence length. Flexural rigidity (product EI) is a structural characteristic of actin filaments that indicates their capacity to withstand bending deformation, where E is Young's modulus, and I is a moment of inertia (depends on the geometry). From the force-displacement curves (Fig. 8 c-d), the flexural rigidity (E × I) can be calculated using equation $= \frac{Fl^3}{48\delta}$, where l is the effective length of the filament, F is the bending force applied, and δ is the deflection (here, the linear regime of bending displacement up to 2.5 nm was considered). Fig. 8e shows the flexural rigidity values of PCDA and FCDA filaments at various loading rates based on the SMD simulation results. The average flexural rigidity of the PCDA and FCDA filaments obtained in this study was$(6.77 \pm 1.2) \times 10^{-26}$ Nm^2 and $(9.09 \pm 1.3) \times 10^{-26}$ Nm^2 respectively. Furthermore, the persistence length (lp) is another well-known measure of polymer stiffness, which can be calculated using the equation $l_p = \frac{EI}{k_b T}$, where T is the temperature (kelvin), and k_b is the Boltzmann constant [70]. The average persistence length (lp) of the PCDA and FCDA filaments observed here was 14.6 ± 2.1 μm and 22.3 ± 2.6 μm, respectively. In our previous SMD simulation study on bare F-actin, we showed that the average flexural rigidity and persistence length of bare F-actin is nearly $(8.06 \pm 0.98) \times 10^{-26}$ Nm^2 and 19.4 ± 1.8 μm, respectively. In the present study, our results show that partial cofilin decoration of actin filament resulted in an approximately 17% reduction in flexural rigidity and 23% reduction in persistence length compared to bare F-actin. In contrast, we observed that complete cofilin decoration of the actin filament resulted in a 15% increase in flexural rigidity and a 16 % increase in persistence length compared to bare F-actin. In a prior experimental study, McCullough Brannon R. et al. reported that cofilin binding increases the bending flexibility of F-actins [24]. Our findings that the PCDA filaments have lower flexural rigidity and persistence length than bare F-actin are comparable to this investigation. However, this prior experimental study does not specify whether the actin filaments were partially or fully decorated with cofilins, nor does it investigate the differences in bending response of partially and fully cofilin decorated F-actins. In this regard, we investigated the bending responses of partially and fully cofilin decorated actin filaments separately. Our findings reveal that partially cofilin-decorated F-actin is more flexible and susceptible to severing than fully cofilin-decorated F-actin, which resists bending and has less severing potential.

4. Conclusions

This study utilizes SMD simulations to explore the mechanical properties of bare, partially, and fully cofilin decorated actin filaments. The SMD simulation shows that the PCDA filament displayed the lowest mechanical performance with average tensile strength and Young's modulus of 63.32 MPa and 1.32 ± 0.7 GPa, respectively. While, bare F-actin showed intermediate mechanical behavior with average tensile strength and Young's modulus of 83.8 MPa and 1.96 ± 0.11 GPa, respectively. However, the FCDA filament presented the highest mechanical performance with average tensile strength and Young's modulus of 100.3 MPa and 2.16 ± 0.18 GPa, respectively. The data from SMD simulations revealed that cofilin cluster regions are more rigid than bare regions of the actin filament, implying that cofilin forms a strong cross-link between two adjacent G-actins. This finding is consistent with prior biochemical research on cofilin-mediated actin filament severing, which reported that cofilin-occupied regions are stable. The comparison of filament failure mechanisms in tension revealed that partially cofilin decorated actin filament preferentially severs at the cluster boundary at the pointed end. The severing behavior observed in PCDA filament is linked to the structural, spatial heterogeneity caused by cofilin binding in the F-actin. We observed that the cofilin binding to G-actin causes its outer domain to rotate by roughly 27°. As a result, cofilin induces the formation of mechanically weak regions at cluster boundaries on the filament. Therefore, tensile and bending failures occurred mainly at the cofilin cluster and bare actin boundary towards the pointed end. We identified a hydrophobically active region formed between the α-helix of G-actin (residues 337-348) and α4-helix plus the N-terminus of the cofilin. The hydrophobic interaction in this region may have a critical role in the rotation of the outer domain of G-actin by cofilin, resulting in the development of local discontinuities and the formation of fragile points in the filament. The cofilin-mediated actin filament severing model proposed here explains how the changes in G-actin-G-actin interfaces generated by cofilin binding trigger the severing of filament at the cofilin cluster boundary towards the pointed end side. Further, we also evaluated the mechanical properties of PCDA and FCDA filaments through compressive modulus measurement. The compressive forces cause the compressive deformation of filament subunits (G-actin and cofilin), requiring the breaking of multiple hydrogen bonds together. Considering the initial linear elastic stress-strain response, the obtained average compressive modulus of PCDA and FCDA filament are 1.42 ± 0.2 GPa and 2.01 ± 0.1 GPa, respectively. Individual filament subunit's resistance to compressive deformation and robust cross-linking of cofilin formed between two adjacent G-actins improved the compressive strength of FCDA filament. While the concentration of compressive deformation at

the pointed end cluster boundary slightly reduced the compressive modulus of the PCDA filament in comparison to the previously reported compressive modulus of bare F-actin. We performed three-point bending tests on filament models to determine their flexural rigidity and persistent length. The average flexural rigidity of the PCDA and FCDA filaments observed in this investigation was $(6.77 \pm 1.2) \times 10^{-26}$ Nm^2 and$(9.09 \pm 1.3) \times 10^{-26}$ Nm^2 respectively. Similarly, the average persistence length (lp) of the PCDA and FCDA filaments observed in this study was 14.6 ± 2.1 μm and 22.3 ± 2.6 μm, respectively. When we compared the peak forces necessary for PCDA filament fragmentation in tension and bending, we discovered that bending deformation and failure is the most efficient mechanism of filament severing by cofilin. The SMD simulations shown here represent a quantitative relation between forces required for actin filament fragmentation with various loading conditions and demonstrate how cofilin-induced local variation in mechanical strength of the filament can modify the severing efficiency and location of the fracture in the filament. This work provides a rich view into the F-actin severing mechanisms initiated by ADF/cofilin and captures the cascade of events that lead to the fragility of the F-actin under conceivable loading paths it may experience.

CRediT authorship contribution statement

Sharad V. Jaswandkar: Methodology, Validation, Formal analysis, Investigation, Writing – original draft. **Kalpana S. Katti:** Supervision, Project administration, Funding acquisition, Writing – review & editing. **Dinesh R. Katti:** Conceptualization, Validation, Writing – review & editing, Supervision, Project administration, Funding acquisition.

Declaration of Competing Interest

The authors declare that they have no known competing financial interests or personal relationships that could have appeared to influence the work reported in this paper.

Acknowledgments

This work is made possible by the support of the National Science Foundation under NSF EPSCoR Track-1 Cooperative Agreement OIA #1946202. NSF grants #1229316 and #2019077 are acknowledged for the support of the computational resources at NDSU CCAST.

Appendix A. Supplementary data

Supplementary data includes 3 figures. Schematic of deformation profiles and failure mechanism of bare F-actin (Fig. 1 a-b), hydrogen bond analysis in PCDA and FCDA filaments during compression tests (Fig. 2 a-f), hydrogen bond analysis in PCDA and FCDA filaments during bending tests (Fig. 3 a-b). Supplementary data to this article can be found online at https://doi.org/10.1016/j.csbj.2022.07.054.

References

[1] Fletcher DA, Mullins RD. Cell mechanics and the cytoskeleton. Nature 2010;463:485–92. https://doi.org/10.1038/nature08908.
[2] Kar S, Katti DR, Katti KS. Evaluation of quasi-static and dynamic nanomechanical properties of bone-metastatic breast cancer cells using a nanoclay cancer testbed. Sci Rep 2021;11. https://doi.org/10.1038/s41598-021-82664-9.
[3] Molla MDS, Katti DR, Katti KS. Mechanobiological evaluation of prostate cancer metastasis to bone using an in vitro prostate cancer testbed. J Biomech 2021;114:. https://doi.org/10.1016/j.jbiomech.2020.110142110142.
[4] Pollard TD. Actin and actin-binding proteins. Cold Spring Harbor Perspect Biol 2016;8:. https://doi.org/10.1101/cshperspect.a018226a018226.
[5] McCall PM, MacKintosh FC, Kovar DR, Gardel ML. Cofilin drives rapid turnover and fluidization of entangled F-actin. Proc Natl Acad Sci 2019;116:12629–37. https://doi.org/10.1073/pnas.1818808116.
[6] Fass J, Gehler S, Sarmiere P, Letourneau P, Bamburg JR. Regulating filopodial dynamics through actin-depolymerizing factor/cofilin. Anat Sci Int 2004;79:173–83. https://doi.org/10.1111/j.1447-073x.2004.00087.x.
[7] Ono S. Mechanism of depolymerization and severing of actin filaments and its significance in cytoskeletal dynamics. Int Rev Cytol 2007:1–82. https://doi.org/10.1016/s0074-7696(07)58001-0.
[8] Pollard TD, Borisy GG. Cellular motility driven by assembly and disassembly of actin filaments. Cell 2003;112:453–65. https://doi.org/10.1016/s0092-8674(03)00120-x.
[9] Loisel TP, Boujemaa R, Pantaloni D, Carlier M-F. Reconstitution of actin-based motility of Listeria and Shigella using pure proteins. Nature 1999;401:613–6. https://doi.org/10.1038/44183.
[10] Dumpich M, Mannherz H, Theiss C. VEGF signaling regulates cofilin and the Arp2/3-complex within the axonal growth cone. Curr Neurovasc Res 2015;12:293–307. https://doi.org/10.2174/1567202612666150603141144.
[11] Tojkander S, Gateva G, Lappalainen P. Actin stress fibers assembly, dynamics and biological roles. J Cell Sci 2012. https://doi.org/10.1242/jcs.098087.
[12] Nakano K, Mabuchi I. Actin-depolymerizing protein Adf1 Is required for formation and maintenance of the contractile ring during cytokinesis in fission yeast. Mol Biol Cell 2006;17:1933–45. https://doi.org/10.1091/mbc.e05-09-0900.
[13] Kremneva E, Makkonen M, Skwarek-Maruszewska A, Gateva G, Michelot A, Dominguez R, et al. Cofilin-2 controls actin filament length in muscle sarcomeres. Dev Cell 2014;31:215–26. https://doi.org/10.1016/j.devcel.2014.09.002.
[14] Bamburg JR. Proteins of the ADF/cofilin family: essential regulators of actin dynamics. Annu Rev Cell Dev Biol 1999;15:185–230. https://doi.org/10.1146/annurev.cellbio.15.1.185.
[15] Carlier M-F, Laurent V, Santolini J, Melki R, Didry D, Xia G-X, et al. Actin depolymerizing factor (ADF/Cofilin) enhances the rate of filament turnover: implication in actin-based motility. J Cell Biol 1997;136:1307–22. https://doi.org/10.1083/jcb.136.6.1307.
[16] Maciver SK, Zot HG, Pollard TD. Characterization of actin filament severing by actophorin from Acanthamoeba castellanii. J Cell Biol 1991;115:1611–20. https://doi.org/10.1083/jcb.115.6.1611.
[17] la Cruz EMD. Cofilin binding to muscle and non-muscle actin filaments: isoform-dependent cooperative interactions. J Mol Biol 2005;346:557–64. https://doi.org/10.1016/j.jmb.2004.11.065.
[18] Andrianantoandro E, Pollard TD. Mechanism of actin filament turnover by severing and nucleation at different concentrations of ADF/cofilin. Mol Cell 2006;24:13–23. https://doi.org/10.1016/j.molcel.2006.08.006.
[19] Cao W, Goodarzi JP, la Cruz EMD. Energetics and kinetics of cooperative cofilinactin filament interactions. J Mol Biol 2006;361:257–67. https://doi.org/10.1016/j.jmb.2006.06.019.
[20] Gressin L, Guillotin A, Guérin C, Blanchoin L, Michelot A. Architecture dependence of actin filament network disassembly. Curr Biol 2015;25:1437–47. https://doi.org/10.1016/j.cub.2015.04.011.
[21] McGough A, Pope B, Chiu W, Weeds A. Cofilin changes the twist of F-actin: implications for actin filament dynamics and cellular function. J Cell Biol 1997;138:771–81. https://doi.org/10.1083/jcb.138.4.771.
[22] Galkin VE, Orlova A, Kudryashov DS, Solodukhin A, Reisler E, Schröder GF, et al. Remodeling of actin filaments by ADF/cofilin proteins. Proc Natl Acad Sci 2011;108:20568–72. https://doi.org/10.1073/pnas.1110109108.
[23] Galkin VE, Orlova A, Lukoyanova N, Wriggers W, Egelman EH. Actin depolymerizing factor stabilizes an existing state of F-actin and can change the tilt of F-actin subunits. J Cell Biol 2001;153:75–86. https://doi.org/10.1083/jcb.153.1.75.
[24] McCullough BR, Blanchoin L, Martiel J-L, la Cruz EMD. Cofilin increases the bending flexibility of actin filaments: implications for severing and cell mechanics. J Mol Biol 2008;381:550–8. https://doi.org/10.1016/j.jmb.2008.05.055.
[25] Prochniewicz E, Janson N, Thomas DD, la Cruz EMD. Cofilin increases the torsional flexibility and dynamics of actin filaments. J Mol Biol 2005;353:990–1000. https://doi.org/10.1016/j.jmb.2005.09.021.
[26] Jaswandkar S, Faisal HMN, Katti KS, Katti DR. Dissociation mechanisms of G-actin subunits govern deformation response of actin filament. Biomacromolecules 2021;22:907–17. https://doi.org/10.1021/acs.biomac.0c01602.
[27] la Cruz EMD, Gardel ML. Actin mechanics and fragmentation. J Biol Chem 2015;290:17137–44. https://doi.org/10.1074/jbc.r115.636472.
[28] Suarez C, Roland J, Boujemaa-Paterski R, Kang H, McCullough B, Reymann A-C, et al. Cofilin tunes the nucleotide state of actin filaments and severs at bare and decorated segment boundaries. Curr Biol 2011;21:862–8. https://doi.org/10.1016/j.cub.2011.03.064.
[29] Bibeau JP, Gray S, la Cruz EMD. Clusters of a few bound cofilins sever actin filaments. J Mol Biol 2021;433:. https://doi.org/10.1016/j.jmb.2021.166833166833.
[30] Wioland H, Guichard B, Senju Y, Myram S, Lappalainen P, Jégou A, et al. ADF/cofilin accelerates actin dynamics by severing filaments and promoting their depolymerization at both ends. Curr Biol 2017;27:1956–1967.e7. https://doi.org/10.1016/j.cub.2017.05.048.

[31] De La Cruz E, Martiel J-L, Blanchoin L. Mechanical heterogeneity favors fragmentation of strained actin filaments. Biophys J 2015;108:2270–81. https://doi.org/10.1016/j.bpj.2015.03.058.
[32] Tanaka K, Takeda S, Mitsuoka K, Oda T, Kimura-Sakiyama C, Maéda Y, et al. Structural basis for cofilin binding and actin filament disassembly. Nat Commun 2018;9. https://doi.org/10.1038/s41467-018-04290-w.
[33] Fan J, Saunders MG, Haddadian EJ, Freed KF, la Cruz EMD, Voth GA. Molecular origins of cofilin-linked changes in actin filament mechanics. J Mol Biol 2013;425:1225–40. https://doi.org/10.1016/j.jmb.2013.01.020.
[34] Faisal HMN, Katti KS, Katti DR. Differences in interactions within viral replication complexes of SARS-CoV-2 (COVID-19) and SARS-CoV coronaviruses control RNA replication ability. JOM 2021. https://doi.org/10.1007/s11837-021-04662-6.
[35] Khan MI, Ferdous SF, Adnan A. Mechanical behavior of actin and spectrin subjected to high strain rate: a molecular dynamics simulation study. Comput Struct Biotechnol J 2021;19:1738–49. https://doi.org/10.1016/j.csbj.2021.03.026.
[36] Lai Y-Y, Li D, Chang S-W. Computational insights into the substrate recognition mechanism of cartilage extracellular matrix degradation. Comput Struct Biotechnol J 2021;19:5535–45. https://doi.org/10.1016/j.csbj.2021.10.002.
[37] Faisal HMN, Katti KS, Katti DR. Binding of SARS-COV-2 (COVID-19) and SARS-COV to human ACE2: Identifying binding sites and consequences on ACE2 stiffness. Chem Phys 2021;551. https://doi.org/10.1016/j.chemphys.2021.111353.
[38] Galkin VE, Orlova A, Salmazo A, Djinovic-Carugo K, Egelman EH. Opening of tandem calponin homology domains regulates their affinity for F-actin. Nature Structural & amp Molecular Biology 2010;17:614–6. https://doi.org/10.1038/nsmb.1789.
[39] Blanchoin L, Pollard TD. Mechanism of interaction of acanthamoeba actophorin (ADF/Cofilin) with actin filaments. J Biol Chem 1999;274:15538–46. https://doi.org/10.1074/jbc.274.22.15538.
[40] Otterbein LR, Graceffa P, Dominguez R. The crystal structure of uncomplexed actin in the ADP state. Science 1979;2001(293):708–11. https://doi.org/10.1126/science.1059700.
[41] Nelson MT, Humphrey W, Gursoy A, Dalke A, Kalé L, Skeel RD, et al. NAMD: a parallel, object-oriented molecular dynamics program. Int J Supercomputer Appl High Perf Comp 1996;10:251–68. https://doi.org/10.1177/109434209601000401.
[42] MacKerell AD, Bashford D, Bellott M, Dunbrack RL, Evanseck JD, Field MJ, et al. All-atom empirical potential for molecular modeling and dynamics studies of proteins. J Phys Chem B 1998;102:3586–616. https://doi.org/10.1021/jp973084f.
[43] Phillips JC, Braun R, Wang W, Gumbart J, Tajkhorshid E, Villa E, et al. Scalable molecular dynamics with NAMD. J Comput Chem 2005;26:1781–802. https://doi.org/10.1002/jcc.20289.
[44] Zhang Y, Feller SE, Brooks BR, Pastor RW. Computer simulation of liquid/liquid interfaces. I. Theory and application to octane/water. J Chem Phys 1995;103:10252–66. https://doi.org/10.1063/1.469927.
[45] Martyna GJ, Tobias DJ, Klein ML. Constant pressure molecular dynamics algorithms. J Chem Phys 1994;101:4177–89. https://doi.org/10.1063/1.467468.
[46] Kim JI, Kwon J, Baek I, Na S. Steered molecular dynamics analysis of the role of cofilin in increasing the flexibility of actin filaments. Biophys Chem 2016;218:27–35. https://doi.org/10.1016/j.bpc.2016.08.002.
[47] Kim JI, Kwon J, Baek I, Park HS, Na S. Cofilin reduces the mechanical properties of actin filaments: approach with coarse-grained methods. PCCP 2015;17:8148–58. https://doi.org/10.1039/c4cp06100d.
[48] Schramm AC, Hocky GM, Voth GA, Blanchoin L, Martiel J-L, la Cruz EMD. Actin filament strain promotes severing and cofilin dissociation. Biophys J 2017;112:2624–33. https://doi.org/10.1016/j.bpj.2017.05.016.
[49] Bibeau JP, Gray S, de La Cruz EM. Clusters of a few bound cofilins sever actin filaments. J Mol Biol 2021;433:. https://doi.org/10.1016/j.jmb.2021.166833166833.
[50] Janmey PA, Euteneuer U, Traub P, Schliwa M. Viscoelastic properties of vimentin compared with other filamentous biopolymer networks. J Cell Biol 1991;113:155–60. https://doi.org/10.1083/jcb.113.1.155.
[51] Fujii T, Iwane AH, Yanagida T, Namba K. Direct visualization of secondary structures of F-actin by electron cryomicroscopy. Nature 2010;467:724–8. https://doi.org/10.1038/nature09372.
[52] Elam WA, Kang H, la Cruz EMD. Biophysics of actin filament severing by cofilin. FEBS Lett 2013;587:1215–9. https://doi.org/10.1016/j.febslet.2013.01.062.
[53] Moriyama K, Yahara I. The actin-severing activity of cofilin is exerted by the interplay of three distinct sites on cofilin and essential for cell viability. Biochem J 2002;365:147–55. https://doi.org/10.1042/bj20020231.
[54] Huehn A, Cao W, Austin Elam W, Liu X, de La Cruz EM, Sindelar C, et al. The actin filament twist changes abruptly at boundaries between bare and cofilin-decorated segments. J Biol Chem 2018;293:5377–83. https://doi.org/10.1074/jbc.AC118.001843.
[55] Wong DY, Sept D. The interaction of cofilin with the actin filament. J Mol Biol 2011;413:97–105. https://doi.org/10.1016/j.jmb.2011.08.039.
[56] Giménez-Andrés M, Čopič A, Antonny B. The many faces of amphipathic helices. Biomolecules 2018;8:45. https://doi.org/10.3390/biom8030045.
[57] Drin G, Antonny B. Amphipathic helices and membrane curvature. FEBS Lett 2009;584:1840–7. https://doi.org/10.1016/j.febslet.2009.10.022.
[58] Pérez-Payá E, Houghten RA, Blondelle SE. The role of amphipathicity in the folding, self-association and biological activity of multiple subunit small proteins. J Biol Chem 1995;270:1048–56. https://doi.org/10.1074/jbc.270.3.1048.
[59] Kessel A, Ben-Tal N. Introduction to proteins. CRC Press; 2010. 10.1201/b10456.
[60] Pace CN, Fu H, Fryar KL, Landua J, Trevino SR, Shirley BA, et al. Contribution of hydrophobic interactions to protein stability. J Mol Biol 2011;408:514–28. https://doi.org/10.1016/j.jmb.2011.02.053.
[61] Camilloni C, Bonetti D, Morrone A, Giri R, Dobson CM, Brunori M, et al. Towards a structural biology of the hydrophobic effect in protein folding. Sci Rep 2016;6. https://doi.org/10.1038/srep28285.
[62] Dyson HJ, Wright PE, Scheraga HA. The role of hydrophobic interactions in initiation and propagation of protein folding. Proc Natl Acad Sci 2006;103:13057–61. https://doi.org/10.1073/pnas.0605504103.
[63] Blanchoin L, Boujemaa-Paterski R, Sykes C, Plastino J. Actin dynamics, architecture, and mechanics in cell motility. Physiol Rev 2014;94:235–63. https://doi.org/10.1152/physrev.00018.2013.
[64] Pollard TD, Cooper JA. Actin, a central player in cell shape and movement. Science 1979;2009(326):1208–12. https://doi.org/10.1126/science.1175862.
[65] Kang H, Bradley MJ, Cao W, Zhou K, Grintsevich EE, Michelot A, et al. Site-specific cation release drives actin filament severing by vertebrate cofilin. Proc Natl Acad Sci 2014;111:17821–6. https://doi.org/10.1073/pnas.1413397111.
[66] McCullough B, Grintsevich E, Chen C, Kang H, Hutchison A, Henn A, et al. Cofilin-linked changes in actin filament flexibility promote severing. Biophys J 2011;101:151–9. https://doi.org/10.1016/j.bpj.2011.05.049.
[67] Huehn AR, Bibeau JP, Schramm AC, Cao W, Cruz EMD la, Sindelar C v. Structures of cofilin-induced structural changes reveal local and asymmetric perturbations of actin filaments. Proc Natl Acad Sci 2020;117:1478–84. https://doi.org/10.1073/pnas.1915987117.
[68] Bourne JW, Torzilli PA. Molecular simulations predict novel collagen conformations during cross-link loading. Matrix Biol 2011;30:356–60. https://doi.org/10.1016/j.matbio.2011.03.010.
[69] Buehler M, Keten S, Ackbarow T. Theoretical and computational hierarchical nanomechanics of protein materials: deformation and fracture. Prog Mater Sci 2008;53:1101–241. https://doi.org/10.1016/j.pmatsci.2008.06.002.
[70] Buehler MJ. Atomistic and continuum modeling of mechanical properties of collagen: elasticity, fracture, and self-assembly. J Mater Res 2006;21:1947–61. https://doi.org/10.1557/jmr.2006.0236.